Transformation microstructures in pyrolite under stress: Implications for anisotropy in subducting slabs below the 660 km discontinuity

Jeffrey-Phillip Gay, Estelle Ledoux, Matthias Krug, Julien Chantel, Anna Pakhomova, Hanns-Peter Liermann, Carmen Sanchez-Valle, Sébastien Merkel

Transformation microstructures in pyrolite under stress: Implications for anisotropy in subducting slabs below the 660 km discontinuity

Jeffrey P. Gay [a,*], Estelle Ledoux [a], Matthias Krug [b], Julien Chantel [a], Anna Pakhomova [c], Hanns-Peter Liermann [c], Carmen Sanchez-Valle [b], Sébastien Merkel [a,*]

[a] Univ. Lille, CNRS, INRAE, Centrale Lille, UMR 8207 - UMET - Unité Matériaux et Transformations, Lille, F-59000, France
[b] Institute for Mineralogy, University of Münster, Münster, D 48149, Germany
[c] Deutsches Elektronen-Synchrotron DESY, Notkestr. 85, Hamburg, 22607, Germany

ABSTRACT

The '660' discontinuity is often associated with a phase transitions in pyrolite at about 24 GPa. There are ubiquitous reports of seismic anisotropy below the '660' which are difficult to explain from a mineralogical point of view. In this study, we implement multigrain crystallography X-ray diffraction in the laser-heated diamond anvil cell in order to track microstructures induced by phase transitions at the pressure and temperature conditions of the discontinuity. Before the onset of transformation, garnet is isotropic with ringwoodite displaying a weak 001 texture. After the transformation, bridgmanite displays strong 001 transformation textures which we attribute to growth under stress. Davemaoite exhibits weak maxima in 101 and 111 orientations with ferropericlase displaying no texture. The results are used to model anisotropy in a subducting slab, with a prediction of no anisotropy above the '660' and up to 1.28% (0.08 km/s) shear wave splitting below the '660'. In addition, we predict $V_{SV} > V_{SH}$ for horizontally traveling waves and near-vertical subduction and $V_{SV} < V_{SH}$ in the case a slab impinging below the boundary layer.

© 2023 The Author(s). Published by Elsevier B.V. This is an open access article under the CC BY license (http://creativecommons.org/licenses/by/4.0/).

1. Introduction

The '660' discontinuity serves as a boundary between the transition zone and lower mantle at approximately 660 km depth within the Earth's mantle. This discontinuity has been observed in several seismological studies by using a variety of reflected and transmitted waveforms (Xu et al., 2003; Deuss et al., 2006; Deuss, 2009); however, some waveforms, including underside P-wave reflections and long period PP precursors, are less successful at detecting reflections at relevant depths (Day and Deuss, 2013; Waszek et al., 2021). SS and P'P' precursors have been more successful in detecting an apparent sharp boundary, less than 2 km thick, at the '660' (Xu et al., 2003; Deuss, 2009). These seismic observations occur both regionally (Wang and Niu, 2010; Jenkins et al., 2016) and globally (Shearer, 2000; Andrews and Deuss, 2008) within the mantle.

The 660 km discontinuity is also believed to be the result of mineralogical phase transitions in pyrolite (Ringwood, 1991), which is believed to be relevant model composition for the Earth's mantle (Faccenda and Zilio, 2017). Phase transitions of pyrope garnet during experimental diamond anvil cell experiments at conditions relevant to the '660' led to the discovery of (Mg,Fe)SiO$_3$ perovskite (Liu, 1974); which was later discovered in nature in the Tenham L6 chondrite and formally named bridgmanite (Tschauner et al., 2014). Bridgmanite alone comprises approximately 80% of the lower mantle by volume (Ishii et al., 2011; Wang et al., 2015), making it an important phase to investigate when determining how mineralogical microstructures impact phenomena such as seismic anisotropy. Deformation experiments on bridgmanite have been conducted in the past to explore texture development (Merkel et al., 2003; Miyagi and Wenk, 2016; Tsujino et al., 2016), strain weakening (Girard et al., 2016), dislocation microstructures (Cordier et al., 2004; Miyajima et al., 2009), flow laws (Tsujino et al., 2022), and grain growth (Yamazaki et al., 2009). However, there are no documented in-situ experiments that investigate transformation microstructures, including grain statistics, immediately before and after the '660' transition in polycrystalline pyrolite samples.

Seismic anisotropy, the directional dependence of seismic wave velocity, has been observed within the Earth's interior and can bring further information on processes at those depths (Long

---

* Corresponding authors.
E-mail addresses: jeffrey-phillip.gay@univ-lille.fr (J.P. Gay), sebastien.merkel@univ-lille.fr (S. Merkel).

and Becker, 2010). Anisotropy can be detected using multiple approaches. Surface waves in upper mantle regimes provides large-scale information on azimuthal anisotropy (Beller and Chevrot, 2020); however shear wave splitting is more commonly used due to the straightforward measurement process (Long and Becker, 2010); although such measurements may lack vertical resolution. Seismic anisotropy within the deep mantle, however, is widely debated, as it is observed locally below '660' in some studies (Wookey et al., 2002; Ferreira et al., 2019; Agrawal et al., 2020; Montagner et al., 2021), but is absent in other more global models (Meade et al., 1995; Panning and Romanowicz, 2006; Panning et al., 2010). The study of seismic anisotropy is largely motivated by providing constraints on deformation within the Earth's interior and interpreting mantle flow processes, but questions remain on its microscopic origin around the '660' discontinuity.

In this study, a series of laser heated diamond anvil cell (DAC) experiments were performed on polycrystalline samples of pyrolite using high energy X-rays from a synchrotron source. Multigrain X-ray diffraction (MGC) is employed in order to track the orientation of grains at pressures and temperatures relevant to the conditions both above and below the 660 km discontinuity. More specifically, we report on experimental textures obtained before and after the transformation from (ringwoodite + garnet) to (bridgmanite + Ca-perovskite + ferropericlase). Also note that Ca-perovskite was renamed to davemaoite recently (Tschauner et al., 2021) and we will use this nomenclature in the paper. Our measurements demonstrate that strong transformation textures can be formed in bridgmanite upon synthesis due to the compressive stress applied to the sample. These textures are then employed to model P and S-wave anisotropy within a pyrolitic mantle in the vicinity of the '660' discontinuity. We show that our predictions of anisotropy are consistent with observations and could be used to understand the stress geometry within the pyrolitic portion of a subducting slab. Experimental procedures and a brief overview of data processing techniques will also be discussed.

2. Methods and data analysis

2.1. Sample preparation

We use sintered polycrystalline pyrolite samples as our starting material. Single crystals of natural San-Carlos olivine, pyrope, enstatite, and diopside were ground to a powder by hand with ethanol. The mixed powders were then loaded into a boron-nitride capsule and inserted into a piston-cylinder press to sinter the samples at 2 GPa and 1000 °C for 30 minutes. The product of the sintering is a polycrystalline aggregate with heterogeneous grain size, ranging between <1 μm and 15 μm, and homogeneous phase distribution, as determined by electron backscatter diffraction (EBSD) phase maps as seen in Fig. S1 of the supplements. Note, however, that the sample is converted to an assemblage of ringwoodite and garnet using in-situ laser heating. The starting grain size of the (ringwoodite + garnet) assemblage is hence different from that measured in EBSD. The sintered material was then cut into disks with a diamond wire saw and then polished by hand on both sides using a series of silicon diamond polishing papers until it reached a thickness of ≈10 μm Finally, the sample was coated on both side with 500 nm of platinum using a GATAN 682 Precision Etching and Coating System (PECS) and then cut into 20 μm diameter disks using a laser cutting machine at the Institut de minéralogie, de physique des matériaux et de cosmochimie in Paris, Sorbonne Université.

2.2. Diamond anvil cell

To perform these experiments at the relevant pressure and temperature conditions of the 660 km discontinuity, a remote controlled membrane driven laser heated diamond anvil cell (DAC) was used. The seats and external housing of the assembly have a wide angle window, which allows for image collection at rotation angles $\Delta\omega = \pm 28°$ during multi-grain crystallography (MGC) data collection. We used diamonds with a culet size of 250 μm diameter along with a rhenium gasket, indented to a thickness between 25 μm and 30 μm. A hole 1/3 the diameter of the diamond culet was drilled in the center of the intended gasket using a motorized electric discharge machine or laser cutting machine to serve as a sample chamber. The sintered disks of pyrolite were loaded in a controlled argon gas atmosphere between layers of KCl that served both as thermal insulation for laser heating and as a pressure calibrant. Platinum flakes were also loaded into the gasket to be used as pressure calibrant, but were not used in order to keep the X-ray beam focused on the same part of the sample through the X-ray diffraction data collection during the whole experiment.
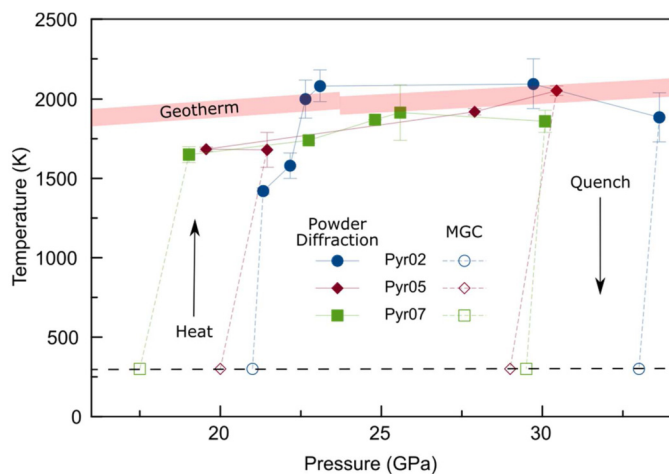
2.3. High pressure/temperature XRD experiments

All experiments were performed at the Extreme Conditions beamline P02.2 at PETRA III (DESY, Hamburg). A schematic of the beamline set up is shown in Fig. 1. We used a monochromatic X-ray beam with a wavelength of 0.2898 Å, and beam dimensions of 1.4 μm (V) × 1.9 μm (H) FWHM, and a Perkin-Elmer XRD 1621 flat panel detector with 2048 × 2048 pixels and a 0.2 × 0.2 mm² pixel size. A CeO₂ powder standard from the National Institute of Standards and Technology (NIST; 674b) was used to calibrate the detector tilt, beam center, and calculate the sample to detector distance (551.262 mm). Double-sided laser heating was carried out using a Yb-fiber laser, 20 μm (FWHM) spot size, to reach the necessary temperatures as installed by default on the beamline and temperatures were determined using spectroradiometry described by Konôpková et al. (2021). Compression and heating of the sample are conducted simultaneously to monitor in situ the transformations in pyrolite at the conditions of the '660'. Pressures and occurrence of the corresponding phases are identified during the experiment using powder diffraction images collected in situ at high P/T and analyzed in the software Dioptas (Prescher and Prakapenka, 2015). The collection of MGC images allows us to observe the evolution of microstructures within the sample upon transformation by providing information on phases present and their associated textures, but requires quenching the sample to ambient T with the layout we used in this work. MGC image collections are taken as close to the transformation conditions as possible.

The first series of MGC images are collected when ringwoodite and garnet form in the DAC at pressures between 18 and 19 GPa and temperatures between 1600 and 1900 K. Once, for instance, ringwoodite and garnet are observed in the powder diffraction pattern, the sample is quenched to ambient T by turning off the laser heating system and a multigrain X-ray diffraction image is taken. Acquisition of the image series happens by rotating the DAC in ω by 0.5° steps from −28° to 28° with collection times of 1 second per image, resulting in a total of 112 images for each MGC scan. After the MGC image collection, the sample is again heated between 1500 and 2000 K and then compressed at high temperature until pressures reach ≈24 GPa. The sample is 'scanned' across the infrared laser in order to induce the phase transformation and homogeneously heat the area of the sample where MGC images are collected; however, the sample position for MGC collections is saved in order to insure the X-ray is sampling the same sample location as previous MGC collections. Heating times could affect grain growth, but were not thoroughly investigated in this work. Once bridgmanite is identified in the powder diffraction pattern, the sample is again quenched and MGC images are collected. During the compression and laser heating process, powder diffraction images are collected without rotation of the DAC.
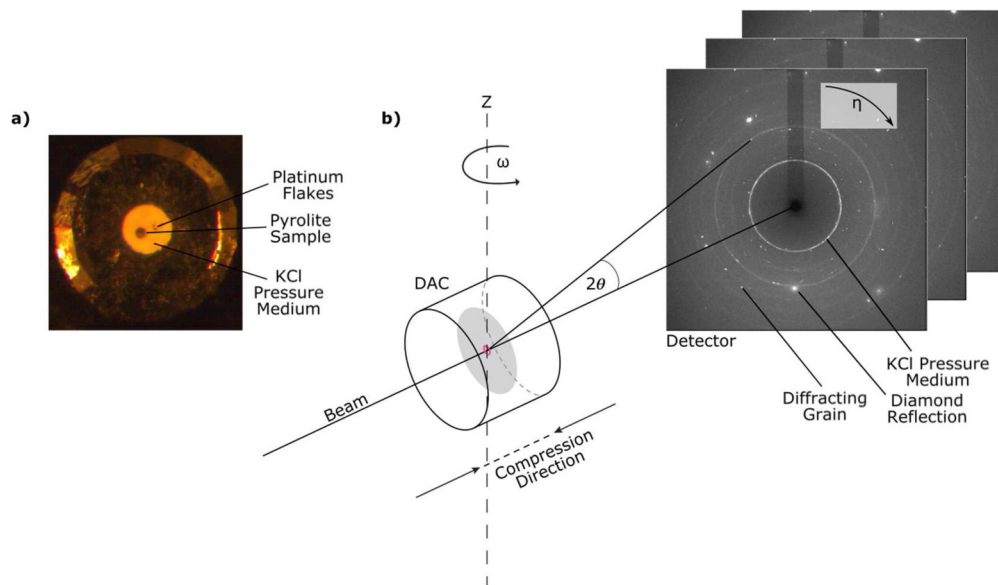
Fig. 1. Experimental setup of multigrain X-ray diffraction at beamline P02.2 at PETRA III (DESY, Hamburg). a) Image of the sample sandwiched between KCl pressure medium along with platinum flakes taken from an optical microscope. b) Overall view of the DAC assembly with X-ray beam passing through the sample in the axial direction. The 2D Perkin-Elmer detector collects diffraction images every 0.5° as the assembly is rotated from −28° to 28° in ω. Actual diffraction images are shown in the insert.

Fig. 2. Pressure-temperature path for three experimental runs Pyr02, Pyr05, and Pyr07. Multigrain images are acquired at 300 K. Open markers are where MCG diffraction data was collected with filled markers indicating where powder diffraction images were taken. Dotted portion of lines along the P/T path denote when the sample is being heated or quenched. Errors in temperature are reported as the deviation from the average values between the upstream and downstream recorded temperature. Black dashed line is a visual aid marking 300 K. Red shaded area marks the geotherm from Katsura et al. (2010). Pressures in KCl, estimated from the equation of state of Tateno et al. (2019), are corrected to account for temperature during laser heating (see text for details).

A total of three separate runs were performed: Pyr02, Pyr05, and Pyr07. Each sample was a separate experiment, with multigrain XRD images collected before and after the transformation to the bridgmanite + davemaoite + ferropericlase assemblage (Fig. 2). Pressure during the experiment is tracked using powder diffraction images and the thermal equation of state of KCl from Tateno et al. (2019). Temperature in KCl is ill-defined because of the temperature gradient between the room temperature diamond and the heated sample, as measured using spectroradiometry. We hence assign the temperature at the mid-point between the diamonds and sample to KCl.

In the three Pyr02, Pyr05, and Pyr07 runs, ringwoodite + garnet assemblages were characterized between 17.5 and 21 GPa at 300 K and then compressed and converted at mantle geotherm

temperatures up to pressures between 29 and 33 GPa. Bridgmanite + davemaoite + ferropericlase assemblages were then characterized using MGC on the quench run-products (Fig. 2).

2.4. Processing MGC data

Analysis of the MGC data is performed using a series of software packages discussed below. Only a brief outline of the process will be provided and more information can be found in Rosa et al. (2015) as well as Langrand et al. (2017). A MGC image collection relies on the measurement of diffraction images at multiple ω angles in order to obtain a comprehensive view of the sample grain orientations in three dimensions. The aim of the procedure is to link the diffraction spots observed in the diffraction images to individual grains within the sample and extract microstructural information such as the number of grains and their orientations. This step is performed using the open-source software package FABLE 3DXRD, which can be found at https://github.com/FABLE-MGC and additional tools specifically designed for this project, TIMEleSS tools, available at https://github.com/FABLE-3DXRD/TIMEleSS. During the first step of the processing, images are cleaned by subtracting the median background from the pressure transmitting medium and masking diamond spots. The median background is calculated using open source TIMEleSS tools. For each pixel on the detector, we calculate the median intensity of all images in a MGC series. The median image is built from those pixel-by-pixel median calculations. The image is then subtracted from each individual image in the MCG series. This method has the advantage of not only subtracting the background noise, but also any reflections that are seen homogeneously in each image including the pressure medium, artifacts on the detector, and some diamond spots. Details on the process are described in the publication of Nisr et al. (2014).

Fig. 3a shows the extracted diffraction peaks in run Pyr05, plotted along the azimuth against inverse d-spacing. Fig. 3c is an example of what diffraction spectra in run Pyr05 look like when the MGC images are averaged and integrated into a 2D pattern, as one would use in powder diffraction. Diffraction peaks with lower intensities are masked by the KCl pressure medium, making it difficult to identify peak locations of garnet, bridgmanite, davemaoite, and ferropericlase phases. Fig. 3b, on the other hand,
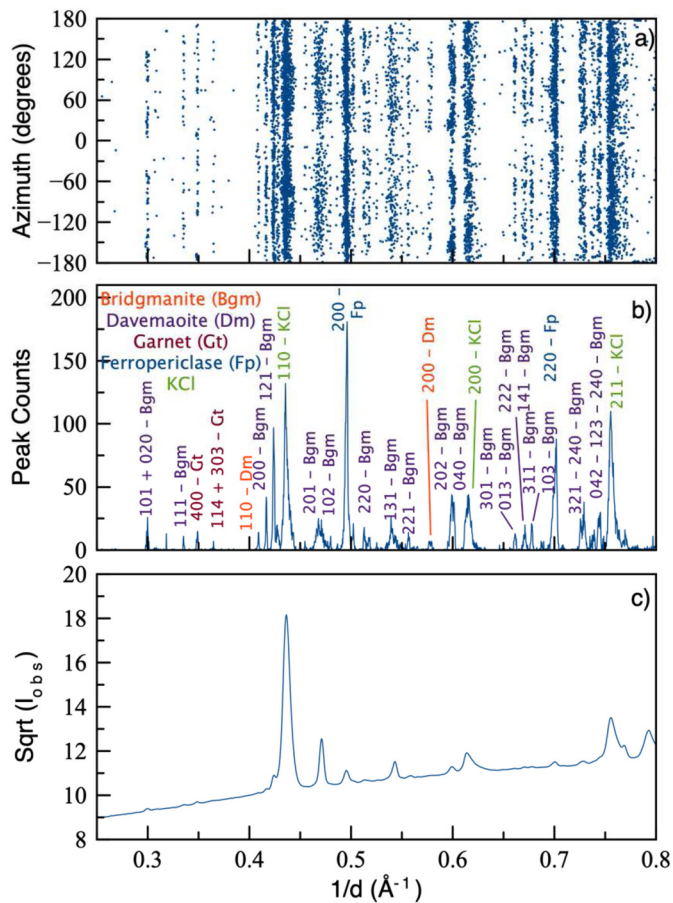
Fig. 3. Experimental diffraction data from run Pyr05 at 29 GPa. a) Extracted diffraction peaks from the 2D diffraction images plotted as a function of azimuth and inverse d-spacing. b) Histogram of the number of extracted single-grain diffraction peaks vs. 1/d. The corresponding phase and Laue indices of each diffraction line are indicated on the figure. c) Diffraction data in MAUD when using an average image of the MGC data collection. The signal is dominated by the pressure medium (KCl) and selected diffraction lines of bridgmanite.

shows a histogram of the number of diffraction spots against inverse d-spacing. Peaks from all phases can be clearly identified. Unit-cell parameters of the mineral phases are then extracted using the software MAUD (Lutterotti et al., 1997). Note the analysis of this spectrum is not a true Rietveld refinement because the data in the histogram is a number of single grain peaks rather than a true peak intensity. It is, however, very efficient at detecting peak positions of phases that would otherwise be drowned out by the KCl pressure medium.

After the peaks are extracted and the phases identified, we use ImageD11 to compute a list of **g**-vectors using the positions of diffraction peaks, refined unit cell parameters, and experimental conditions such as wavelength, sample to detector distance, and detector tilt. In order to avoid incorrectly assigning pressure medium **g**-vectors to sample grains, 2θ ranges that overlap with the pressure medium are excluded from the list. Finally, we use GrainSpotter (Schmidt, 2014) and the list of **g**-vectors, to index grains within the sample by assigning **g**-vectors with matching orientations. To achieve this, GrainSpotter generates a series of randomly oriented grains and computes their corresponding **g**-vectors. GrainSpotter then tries to match each experimentally measured **g**-vector to the generated theoretical **g**-vectors. A **g**-vector is assigned to a grain when the diffraction angles 2θ, η, and ω, shown in Fig. 1, are within the defined tolerances from the theoretical values.

One difficulty arises from having multiple crystalline phases in the sample. This is remedied by running multiple subsequent GrainSpotter indexings for each individual phase, removing indexed **g**-vectors from the list of unassigned **g**-vectors at each step. Additionally, the number of indexed grains is improved by running multiple iterations of GrainSpotter with decreasing tolerances. In the first iterations, tolerances are set to $\sigma_{2\theta} = 0.02°$, $\sigma_\eta = 1.0°$, and $\sigma_\omega = 2.0°$ for each phase. In the last iterations, tolerances are set to $\sigma_{2\theta} = 0.08°$, $\sigma_\eta = 2.0°$, and $\sigma_\omega = 3.0°$ for each phase. This results in the indexing of between 35 and 89% of the **g**-vectors, corresponding to between 44 and 736 sample grains (Table S1). Note that better indexing performance are obtained for samples including bridgmanite, davemaoite, and ferropericlase where between 83 and 89% of the **g**-vectors are assigned. The reason for the lower indexing performance on garnet + ringwoodite assemblages is unclear, but may be due to the large number reflections in both the garnet and ringwoodite structures.

Grain orientations from GrainSpotter are plotted as inverse pole figures (IPF) of the direction of compression using the MTEX toolbox (Bachmann et al., 2010; Mainprice et al., 2014). We use MTEX to fit an orientation distribution function to the list of single grain orientations and plot the results as IPFs. Note that our inverse pole figures refer to directions normal to diffracting planes and hence use Laue indices, with no parenthesis. Each dot on the IPF in Fig. 4 represents a grain indexed, with color corresponding to the probability of a specific orientation, which is plotted using a scale of multiples of random distribution (m.r.d.).

2.5. Elasticity and calculations of seismic anisotropy

Phase proportions in pyrolite, both before and after transformation, were calculated using the software package HeFESTo (Stixrude and Lithgow-Bertelloni, 2010) available at https://github.com/stixrude/HeFESToRepository. Above the '660', at conditions of 22 GPa and 1700 K, pyrolite is composed of 67% ringwoodite, 25% garnet, and 8% other minor phases by volume. Below the '660', at 27 GPa and 1900 K, pyrolite contains 77% bridgmanite, 17% ferropericlase, and 6% davemaoite by volume. Elastic constants for each phase are required in order to complete calculations of seismic velocities (Table S2).

In this work, garnet and ringwoodite are treated as isotropic materials, which is consistent with measurements on single crystals in the pressure range of the mantle transition zone (MTZ) (Sinogeikin and Bass, 2000; Murakami et al., 2008; Zhou et al., 2022). Studies report moderate elastic anisotropy of ferropericlase at the condition of the MTZ (Jackson et al., 2006; Yang et al., 2016; Fan et al., 2019; Immoor et al., 2022). Additionally, in our experiments we observe no texture, therefore we also treat ferropericlase as an elastically isotropic material.

Both bridgmanite and davemaoite are elastically anisotropic at mid-mantle conditions (Kurnosov et al., 2018; Fu et al., 2019; Criniti et al., 2021; Li et al., 2006) and will hence be treated to include the effect of anisotropy. Anisotropic elastic properties for textured polycrystals, pyrolite assemblage, and the corresponding wave velocities and anisotropy are then calculated using experimental texture data with MTEX and will be described later.

3. Results

3.1. Transformation microstructures in pyrolite

3.1.1. Grain indexing statistics

Grains are indexed before and after the phase transformation takes place in our experiments. Before the transition, we index ringwoodite and garnet phases simultaneously, which results in between 107 and 120 indexed grains between the two phases.
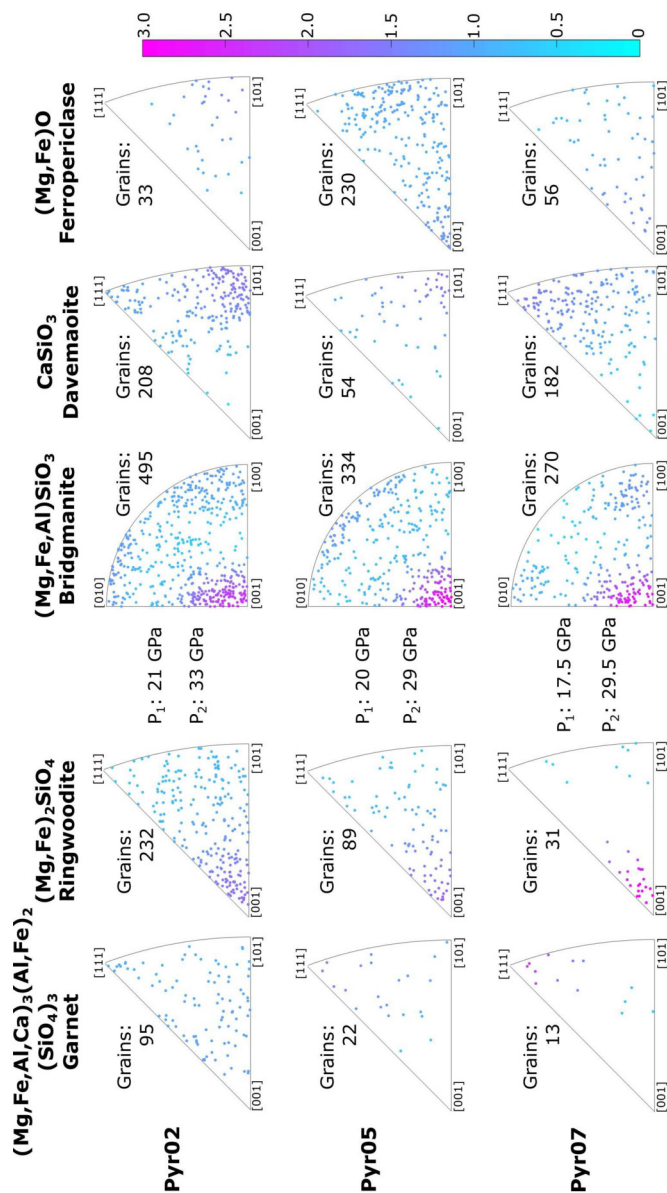
Fig. 4. Inverse pole figures of the compression direction for runs Pyr02, Pyr05, and Pyr07 showing individual grain orientations of $Mg_3Al_2(SiO_4)_3$ garnet and $(Mg,Fe)_2SiO_4$ ringwoodite before transformation and $(Mg,Fe)SiO_3$ bridgmanite, $CaSiO_3$ davemaoite, and $(Mg,Fe)O$ ferropericlase after complete transformation in a pyrolitic composition. Equal area projection. Grains are colored according to an orientation distribution fitted for each phase and color scale in multiples of random distribution (m.r.d.). P_1 indicates the pressure before transformation and P_2 the pressure after transformation. The number of indexed grains is indicated above each inverse pole figure.

After the transition we see a marked increase in the amount of grains indexed for phases bridgmanite, davemaoite, and ferropericlase. Here we are able to index between 508 and 736 grains amongst the three phases. Our indexing strategy leads to between 35 and 89% of all relevant **g**-vectors assigned to individual grains. For instance, 84% of the relevant **g**-vectors in Fig. 3 have been assigned. For more details on grain indexing capabilities please refer to the Supplementary Materials and Table S1.

3.1.2. Experimental textures in pyrolite phases

Fig. 4 shows grain orientations of ringwoodite and garnet before transformation; and bridgmanite, davemaoite, and ferropericlase after the transformation. In all runs, ringwoodite displays a 001 compression texture with m.r.d. values between 1.7 and 2.8.

The garnet phase, however, is randomly oriented in all runs. After the transformation, bridgmanite exhibits strong preferred orientation in 001 along the compression axis with m.r.d. values between 2.7 and 3. Transformation textures in davemaoite varies between the three experimental runs. In run Pyr02 and Pyr05, weak 101 orientations can be observed. Whereas in run Pyr07, the orientations are more diffuse, with the majority of grains oriented in 111. M.r.d. values of the davemaoite phase across all three runs are the same; with maximum values of 1.6. Finally, ferropericlase exhibits a random texture throughout all three runs. The texture results in Fig. 4 could be improved by accounting for grain size distributions of the indexed grains, but this is not achievable with the current dataset. Nevertheless, we are confident that the main signal from the dataset, i.e., the strong 001 synthesis texture in bridgmanite is not affected by this bias.

3.2. Seismic wave velocities above and below the '660' discontinuity

3.2.1. Bridgmanite and davemaoite

Both bridgmanite and davemaoite are anisotropic and display strong transformation textures; therefore they must be considered during the calculations of seismic anisotropy. Single-crystal elastic constants for bridgmanite and davemaoite were interpolated to 1900 K and 27 GPa from the results of Luo et al. (2021) and Li et al. (2006). We then used MTEX to generate a model texture matching the results of the experiments and to calculate the corresponding polycrystal elastic properties and seismic velocities. The details of the procedure, along with the single crystal and polycrystal elastic moduli and the corresponding seismic velocity plots can be found in the supplements (Section S3, Table S2, Fig. S2).

3.2.2. Anisotropy in a compressed pyrolite polycrystal before and after transformation

As mentioned in section 2.5, garnet and ringwoodite phases are both seismically isotropic in V_P and V_S at 22 GPa and 1700 K. Ferropericlase is also assumed to be elastically isotropic at 27 GPa and 1900 K based on the lack of texture in our experimental data. Nevertheless, they contribute to seismic velocities in the pyrolite polycrystal. We use MTEX and the phase proportions in section 2.5 to compute the velocities in a pyrolite polycrystal both above and below the '660'.

For the pyrolite polycrystal above '660' (Fig. 5), there is zero anisotropy in V_S and V_P with mean P-wave velocity of 10.08 km/s. For the pyrolite polycrystal below the transition, however, maximum S-wave splitting is 1.28% (0.08 km/s) for waves traveling perpendicular to compression. S-waves are vertically polarized where splitting is maximum. For P-waves, mean velocity is 10.83 km/s, ranging between 10.82 km/s for waves traveling parallel to compression to 10.84 km/s for waves traveling perpendicular to compression, resulting in 0.17% P-wave azimuthal anisotropy.

4. Discussion

4.1. Pre-transformation textures

At mantle conditions above the 660 km discontinuity, ringwoodite and garnet make up approximately 93% by volume of phases within pyrolite samples at pressures and temperatures of 22 GPa and 1700 K respectively, as calculated by HeFESTo. Ringwoodite is 67% by volume of the total, making it the dominant phase. In all experiments, ringwoodite displays 001 preferred orientations, where (001) planes align perpendicular to the compression axis; however, the texture strength in run Pyr07 is much stronger, with a m.r.d. value of 3 in Fig. 4. It is likely that the stronger texture observed in run Pyr07 is a result of only 31 indexed grains compared to 232 in Pyr02 and 89 in Pyr05. This can
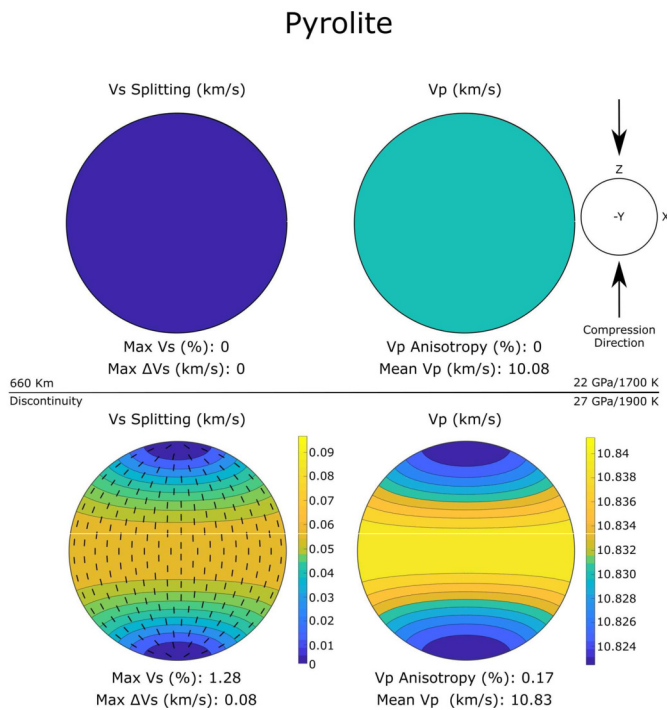
Pyrolite

Fig. 5. Seismic velocities in pyrolite at conditions above and below the 660 km discontinuity. Both V_S splitting and V_P anisotropy are plotted in units of km/s. Black tick marks in V_S anisotropy plots indicate the fast shear wave polarization direction. Plots are oriented so that compression is in the vertical direction. Details on their calculations and numerical values of the corresponding densities and elastic moduli are provided in the Supplementary Materials.

lead to an overestimation of intensity in the orientation distribution function. With a larger number of grains, orientations are distributed amongst more grains resulting in lower texture strengths. Therefore, we conclude the stronger texture in run Pyr07 is due to the low number of grains and not representative of the true texture strength. The difference in amount of ringwoodite grains indexed between the Pyr02, Pyr05, and Pyr07 is probably a result of grain size differences in each sample, which would lead to a different number of indexed grains. Past DAC and D-DIA experiments have reported 101 compression textures in ringwoodite (Wenk et al., 2004, 2005); however, in a study by Miyagi and Wenk (2016) ringwoodite displays a maximum in 101 with a weaker maximum in 001 orientations before the transformation to (bridgmanite + ferropericlase). Although we do not observe the same 101 textures in the ringwoodite phase of our experiments, DAC experiments in Wenk et al. (2004) and D-DIA experiments in Wenk et al. (2005) were conducted at room temperature. Additionally, none of these experiments use a pyrolitic starting material.

The garnet phase of our pyrolite accounts for 25% by volume of the phases at pretransformation conditions. Across all three runs garnet remains isotropic in texture (Fig. 4). Recent radial diffraction experiments investigating texture development in garnet report weak texture in (001) orientations perpendicular to compression at ambient temperatures (Vennari et al., 2021). Other studies on the plasticity of garnet have been conducted and found the resistance to plastic flow in garnet to be significantly higher than in other mantle minerals (Karato et al., 1995), while others argue garnet to actually be weaker than other mantle phases such as ringwoodite within the transition zone (Kavner, 2007). Our explanation for the lack of texture development in garnet during compression is simply due to the weak deformation textures in garnet and the fact that we did not apply much strain in this sample.

4.2. Post-transformation textures

The three dominant phases in pyrolite after transformation at the '660' are bridgmanite, davemaoite, and ferropericlase. Bridgmanite makes up 77% by volume of pyrolite at conditions of 27 GPa and 1900 K as reported by HeFESTo. Bridgmanite exhibits texture in (001) planes (Pbnm setting) perpendicular to the compression axis with m.r.d. values up to 3. Few studies have investigated transformation textures in bridgmanite; however, our results compare well with textures observed in radial diffraction experiments by Miyagi and Wenk (2016), where bridgmanite transformed from enstatite displays 001 texture at 31 GPa. Transformation from pure olivine to (bridgmanite + ferropericlase), however, results in a diffuse maximum spread between 001 and 100 orientations at 33 GPa as seen in Fig. 3b of Miyagi and Wenk (2016). Another study by Wenk et al. (2006), also shows a difference in bridgmanite transformation textures depending on the pre-transformation phase. Bridgmanite transformed from olivine in a DAC, reveals 100 orientations perpendicular to compression at 25 GPa; however, when bridgmanite is transformed from enstatite at 44 GPa there is a strong maximum in 001 orientations. Additionally, in the same study, Wenk et al. (2006) observes an intermediate maximum in 101 orientations when bridgmanite is transformed from pure ringwoodite at 43 GPa.

Experimental transformation textures of bridgmanite are unrelated to known slip systems. Past multianvil deformation studies have documented (100) slip in [001] in pure bridgmanite at conditions of the uppermost lower mantle (Tsujino et al., 2016). At higher pressure, but below 55 GPa, the dominant slip plane is reported to be (100) resulting in a 100 deformation texture at 300 K (Merkel et al., 2003; Miyagi and Wenk, 2016). X-ray diffraction analysis of dislocations by Cordier et al. (2004) on recovered bridgmanite samples, deformed in the multianvil press, report slip in (001)[100] and (001)[010]. Few of these previous results on deformation and slip systems in bridgmanite would result in preferred orientation of (001) planes perpendicular to compression as observed here. In addition, we applied very little strain in the sample post phase transformation. We hence conclude that our measured experimental textures are a result of oriented growth under stress rather than deformation.

Davemaoite also exhibits transformation textures in 101 and 111 orientations pyrolite. The strongest of these textures is observed in run Pyr02 where (101) planes orient perpendicular to compression. This same texture is found in run Pyr05, however, significantly less grains are indexed; 208 grains in Pyr02 versus 54 grains in Pyr05. run Pyr07 displays a different texture with 111 planes oriented perpendicular to the compressive axis. Textures in these experiments differ from deformation textures reported in radial diffraction DAC experiments by (Miyagi et al., 2009; Immoor et al., 2022), who report a 100 texture in deformed pure $CaSiO_3$. Again, our experiment are measuring transformation textures in a pyrolitic assemblage and could differ from deformation experiments in a pure phase.

4.3. Implications for anisotropy in subducting slabs

It is believed that subducting slabs in the mantle collide with a more viscous layer around 660 km depth, which would initially apply a compressive stress on the slab (Wookey et al., 2002; Mao and Zhong, 2018). Compositionally, the top outermost portion of the slab is made up of a thin layer of mid-ocean ridge basalt with an underlying layer of harzburgite; however, the majority of the slab is pyrolitic in nature (Faccenda and Zilio, 2017). Therefore, we can consider that our transformation experiments on pyrolite at mantle P/T under compressive stresses are relevant for observations of anisotropy inside subducting slabs.
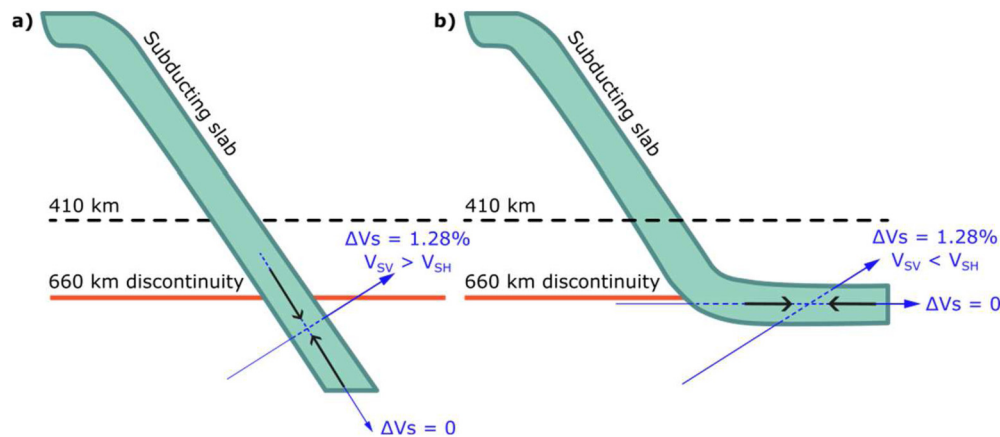
Fig. 6. Scenarios for anisotropy in a subducting slab below the '660'. Blue arrows denote shear wave propagation directions with corresponding splitting values. Black arrows indicate compression direction. a) Subducting slab impinging on the more viscous upper-lower mantle below 660 km depth. b) Subducting slab bending along the 660 km discontinuity creating a horizontal compressive stress.

Our model does not predict anisotropy above the 660 discontinuity. Below 660 km depth, seismic observations report that anisotropy is weak in comparison to shallower depths (Montagner and Kennett, 1996; Ohuchi et al., 2011), where olivine, the dominant mineral in the upper mantle, exhibits significant crystallographic preferred orientation and anisotropy. Nevertheless, anisotropy has been observed below the '660' in studies using surface waves (Yuan and Beghein, 2013; Montagner et al., 2021), body waves (Wookey et al., 2002; Agrawal et al., 2020), and seismic tomography (Ferreira et al., 2019). Where exactly anisotropy is observed, however, remains largely debated with some literature suggesting it is developed mostly around rigid subducting slabs due to high induced strain in the surrounding hot mantle (Ferreira et al., 2019) and others arguing anisotropy is strongest within the slabs where they are most contorted; as the surrounding mantle is largely isotropic (Agrawal et al., 2020). In the discussion below we will try to construct a model to understand these observations and show how our data can help reconcile these observations.

For a vertically compressive stress, we predict that S-waves will show no splitting for waves traveling parallel to compression and 1.28% splitting in waves traveling perpendicular to compression (Fig. 5). Some observations suggest average anisotropy values of 3% just below the '660' assuming anisotropy is confined to a 100 km layer (Wookey et al., 2002); however, in another study by Yuan and Beghein (2013), the root mean square model amplitude at 800 km depth has approximately 1% anisotropy. This is comparable to observations of radial anisotropy within the deep upper mantle in Beghein et al. (2006) and Panning and Romanowicz (2006). Additionally, Montagner et al. (2021), observe fast vertically polarized S-waves ($V_{SV} > V_{SH}$) at 800 km depth below western America, central Africa, and central Asia using surface-wave overtone datasets to generate 3D anisotropy models. In a separate study, Visser et al. (2008) created a 3D model of velocity and radial anisotropy that resulted in $V_{SV} > V_{SH}$ with 1-2% amplitude below the MTZ. Both the results of Visser et al. (2008) and Montagner et al. (2021) are consistent with the scenario proposed in Fig. 6a, where a "vertical" compressive stress is generated within the slab as it passes through the '660' and impinges on the more viscous surrounding mantle material. In this scenario $V_{SV} > V_{SH}$ for S-waves traveling in near horizontal direction, with no splitting in V_S for waves traveling parallel to the slab.

In contrast, the study of Wookey et al. (2002) observes horizontally polarized shear waves leading vertically polarized shear waves, albeit with larger values of V_S anisotropy. Agrawal et al. (2020) reports maximum splitting within the slab for nearly vertically propagating waves. These two are not compatible with a

vertical compressive stress geometry. These observations could be remedied by considering a scenario where a horizontal compressive force is generated within the slab as it bends and travels along the '660', as shown in Fig. 6b. In this scenario $V_{SV} < V_{SH}$ for S-waves traveling perpendicular to the horizontal slab, with no splitting in V_S for waves traveling parallel to the slab.

Other studies investigating anisotropy deeper within the mantle (660-1000 km) suggest fast horizontally polarized waves ($V_{SV} < V_{SH}$) imaged near subducting slabs below 660 km depth (Ferreira et al., 2019) which is consistent with Fig. 6b. For such reports of deep mantle anisotropy, however, deformation textures resulting from slab subduction should also be taken into account as the microstructural imprint of phase transformation is likely to be erased or modified by further deformation.

5. Conclusions

In this paper we presented the results of phase transformation experiments at the pressure and temperature conditions of the 660 km discontinuity on pyrolite. Compression was carried out in a laser-heated DAC at pressures ranging from 17.5 to 33 GPa and temperatures between 1500 and 2000 K; implementing multigrain X-ray diffraction to study the sample. We successfully observe the phase transition from (ringwoodite + garnet) to (bridgmanite + davemaoite + ferropericlase) in all three runs along with the associated microstructures.

Multigrain data processing techniques resulted in the assignment of single crystal diffraction peaks to individual grains within the sample. Our indexing capability ranges from 508 to 736 grains post transformation in a multiphase material. Prior to transformation, garnet is isotropic and ringwoodite is weakly textured with 001 planes oriented perpendicular to the compressive stress. After the transformation is induced, bridgmanite displays strong texture in 001 across all experiments as a result of oriented growth under stress. Davemaoite is moderately textured with 101 orientations in one experiment, and 111 orientations in another. Ferropericlase remains largely untextured in all experiments.

Using single grain elastic constants, calculated at pressures and temperatures relevant to the MTZ, and our measured microstructures we computed P and S-wave anisotropy in a pyrolitic polycrystal both above and below the 660 discontinuity. Our models predict no anisotropy in V_S and V_P above the '660.' Below the '660' S-wave splitting is 1.28% (0.08 km/s) for waves traveling perpendicular to compression and null for waves traveling parallel. P-wave velocities range from 10.82 km/s for waves traveling parallel to compression to 10.84 km/s for waves traveling perpendicular

to compression, resulting in 0.17% azimuthal P-wave anisotropy. Our predicted amplitudes of anisotropy below the '660' in our models are consistent with observations by Beghein et al. (2006); Panning and Romanowicz (2006); Visser et al. (2008); Yuan and Beghein (2013). Our prediction for fast S-wave polarization depends on compression geometry with $V_{SV} > V_{SH}$ for a vertically compressed subducting slab and $V_{SH} > V_{SV}$ for a horizontally compressed slab.

Seismic anisotropy observed below the '660' is still a much debated topic. Here we show that bridgmanite within a pyrolitic material can develop strong textures when formed under stress. Based on these experimental observations, we can then attribute the bulk of anisotropy below the '660' to bridgmanite oriented growth and establish how anisotropy can be used to map stress within a subducting slab in those regions. This study also demonstrates the relevance of high pressure and high temperature multigrain crystallography in the diamond anvil cell for understanding mantle processes. Future work using this technique would prove useful in understanding anisotropy deeper in the mantle, where further plastic deformation would play an important role.

CRediT authorship contribution statement

Jeffrey P. Gay: Formal analysis, Investigation, Writing – original draft. **Estelle Ledoux:** Formal analysis, Investigation. **Matthias Krug:** Formal analysis, Investigation. **Julien Chantel:** Investigation. **Anna Pakhomova:** Investigation. **Hanns-Peter Liermann:** Investigation. **Carmen Sanchez-Valle:** Conceptualization, Funding acquisition, Investigation. **Sébastien Merkel:** Conceptualization, Formal analysis, Funding acquisition, Investigation, Supervision, Writing – review & editing.

Declaration of competing interest

The authors declare that they have no known competing financial interests or personal relationships that could have appeared to influence the work reported in this paper.

Data availability

Data files necessary for grain indexing are availble on Recherche Data Gouv: https://doi.org/10.57745/I0J6LZ (Gay et al., 2023).

Appendix A. Supplementary material

Supplementary material related to this article can be found online at https://doi.org/10.1016/j.epsl.2023.118015.

References

Agrawal, S., Eakin, C.M., Portner, D.E., Rodriguez, E.E., Beck, S.L., 2020. The deformational journey of the Nazca slab from seismic anisotropy. Geophys. Res. Lett. 47, 1–9. https://doi.org/10.1029/2020GL087398.

Andrews, J., Deuss, A., 2008. Detailed nature of the 660 km region of the mantle from global receiver function data. J. Geophys. Res., Solid Earth 113, 1–12. https://doi.org/10.1029/2007JB005111.

Bachmann, F., Hielscher, R., Schaeben, H., 2010. Texture analysis with MTEX-Free and open source software toolbox. In: Solid State Phenomena, pp. 63–68.

Beghein, C., Trampert, J., van Heijst, H.J., 2006. Radial anisotropy in seismic reference models of the mantle. J. Geophys. Res., Solid Earth 111, 1–9. https://doi.org/10.1029/2005JB003728.

Beller, S., Chevrot, S., 2020. Probing depth and lateral variations of upper-mantle seismic anisotropy from full-waveform inversion of teleseismic body-waves. Geophys. J. Int. 222, 352–387. https://doi.org/10.1093/GJI/GGAA069.

Cordier, P., Ung'ar, T., Zsoldos, L., Tichy, G., 2004. Dislocation creep in MgSiO$_3$ perovskite at conditions of the Earth's uppermost lower mantle. Nature 428, 837–840. https://doi.org/10.1038/nature02472.

Criniti, G., Kurnosov, A., Boffa Ballaran, T., Frost, D.J., 2021. Single-crystal elasticity of MgSiO$_3$ bridgmanite to mid-lower mantle pressure. J. Geophys. Res., Solid Earth 126. https://doi.org/10.1029/2020JB020967.

Day, E.A., Deuss, A., 2013. Reconciling PP and P'P' precursor observations of a complex 660 km seismic discontinuity. Geophys. J. Int. 194, 834–838. https://doi.org/10.1093/gji/ggt122.

Deuss, A., 2009. Global observations of mantle discontinuities using SS and PP precursors. Surv. Geophys. 30, 301–326. https://doi.org/10.1007/s10712-009-9078-y.

Deuss, A., Redfern, S.A., Chambers, K., Woodhouse, J.H., 2006. The nature of the 660-kilometer discontinuity in Earth's mantle from global seismic observations of PP precursors. Science 311, 198–201. https://doi.org/10.1126/science.1120020.

Faccenda, M., Zilio, L.D., 2017. The role of solid–solid phase transitions in mantle convection. Lithos 268–271, 198–224. https://doi.org/10.1016/j.lithos.2016.11.007.

Fan, D., Fu, S., Yang, J., Tkachev, S.N., Prakapenka, V.B., Lin, J.F., 2019. Elasticity of single-crystal periclase at high pressure and temperature: the effect of iron on the elasticity and seismic parameters of ferropericlase in the lower mantle. Am. Mineral. 104, 262–275. https://doi.org/10.2138/am-2019-6656.

Ferreira, A.M., Faccenda, M., Sturgeon, W., Chang, S.J., Schardong, L., 2019. Ubiquitous lower-mantle anisotropy beneath subduction zones. Nat. Geosci. 12, 301–306. https://doi.org/10.1038/s41561-019-0325-7.

Fu, S., Yang, J., Tsujino, N., Okuchi, T., Purevjav, N., Lin, J.F., 2019. Single-crystal elasticity of (Al, Fe)-bearing bridgmanite and seismic shear wave radial anisotropy at the topmost lower mantle. Earth Planet. Sci. Lett. 518, 116–126. https://doi.org/10.1016/j.epsl.2019.04.023.

Gay, J., Ledoux, E., Krug, M., Chantel, J., Pakhomova, A., Liermann, H.-P., Sanchez-Valle, C., Merkel, S., 2023. EPSL 2023 on Transformation Microstructures in Pyrolite. Recherche Data Gouv. https://doi.org/10.57745/I0J6LZ.

Girard, J., Amulele, G., Farla, R., Mohiuddin, A., Karato, S.I., 2016. Shear deformation of bridgmanite and magnesiowüstite aggregates at lower mantle conditions. Science 351, 144–147. https://doi.org/10.1126/science.aad3113.

Immoor, J., Miyagi, L., Liermann, H.P., Speziale, S., Schulze, K., Buchen, J., Kurnosov, A., Marquardt, H., 2022. Weak cubic CaSiO$_3$ perovskite in the Earth's mantle. Nature 603, 276–279. https://doi.org/10.1038/s41586-021-04378-2.

Ishii, T., Kojitani, H., Akaogi, M., 2011. Post-spinel transitions in pyrolite and Mg$_2$SiO$_4$ and akimotoite-perovskite transition in MgSiO$_3$: precise comparison by high-pressure high-temperature experiments with multi-sample cell technique. Earth Planet. Sci. Lett. 309, 185–197. https://doi.org/10.1016/j.epsl.2011.06.023.

Jackson, J.M., Sinogeikin, S.V., Jacobsen, S.D., Reichmann, H.J., Mackwell, S.J., Bass, J.D., 2006. Single-crystal elasticity and sound velocities of (Mg$_{0.94}$Fe$_{0.06}$)O ferropericlase to 20 GPa. J. Geophys. Res., Solid Earth 111, 1–8. https://doi.org/10.1029/2005JB004052.

Jenkins, J., Cottaar, S., White, R.S., Deuss, A., 2016. Depressed mantle discontinuities beneath Iceland: evidence of a garnet controlled 660 km discontinuity? Earth Planet. Sci. Lett. 433, 159–168. https://doi.org/10.1016/j.epsl.2015.10.053.

Karato, S.I., Wang, Z., Liu, B., Fujino, K., 1995. Plastic deformation of garnets: systematics and implications for the rheology of the mantle transition zone. Earth Planet. Sci. Lett. 130, 13–30. https://doi.org/10.1016/0012-821X(94)00255-W.

Katsura, T., Yoneda, A., Yamazaki, D., Yoshino, T., Ito, E., Suetsugu, D., Bina, C., Inoue, T., Wiens, D., Jellinek, M., 2010. Adiabatic temperature profile in the mantle. Phys. Earth Planet. Inter. 183, 212–218. https://doi.org/10.1016/j.pepi.2010.07.001.

Kavner, A., 2007. Garnet yield strength at high pressures and implications for upper mantle and transition zone rheology. J. Geophys. Res., Solid Earth 112, 1–9. https://doi.org/10.1029/2007JB004931.

Konôpková, Z., Morgenroth, W., Husband, R., Giordano, N., Pakhomova, A., Gutowski, O., Wendt, M., Glazyrin, K., Ehnes, A., Delitz, J.T., Goncharov, A.F., Prakapenka, V.B., Liermann, H.P., 2021. Laser heating system at the extreme conditions beamline, P02.2, PETRA III. J. Synchrotron Radiat. 28, 1747–1757. https://doi.org/10.1107/S1600577521009231.

Kurnosov, A., Marquardt, H., Frost, D.J., Ballaran, T.B., Ziberna, L., 2018. Elasticity of lower-mantle bridgmanite. Nature 564, E18–E26. https://doi.org/10.1038/s41586-018-0741-7.

Langrand, C., Hilairet, N., Nisr, C., Roskosz, M., Ribárik, G., Vaughan, G.B., Merkel, S., 2017. Reliability of multigrain indexing for orthorhombic polycrystals above 1 Mbar: application to MgSiO₃ post-perovskite. J. Appl. Crystallogr. 50, 120–130. https://doi.org/10.1107/S1600576716018057.

Li, L., Weidner, D.J., Brodholt, J., Alfè, D., Price, G.D., Caracas, R., Wentzcovitch, R., 2006. Elasticity of CaSiO₃ perovskite at high pressure and high temperature. Phys. Earth Planet. Inter. 155, 249–259. https://doi.org/10.1016/j.pepi.2005.12.006.

Liu, L.g., 1974. Silicate perovskite from phase transformations of pyrope-garnet at high pressure and temperature. Geophys. Res. Lett. 1, 277–280.

Long, M.D., Becker, T.W., 2010. Mantle dynamics and seismic anisotropy. Earth Planet. Sci. Lett. 297, 341–354. https://doi.org/10.1016/j.epsl.2010.06.036.

Luo, C., Deng, X., Wang, W., Shukla, G., Wu, Z., Wentzcovitch, R.M., 2021. cij: a Python code for quasiharmonic thermoelasticity. Comput. Phys. Commun. 267, 108067. https://doi.org/10.1016/j.cpc.2021.108067.

Lutterotti, L., Matthies, S., Wenk, H.R., Schultz, A.S., Richardson, J.W., 1997. Combined texture and structure analysis of deformed limestone from time-of-flight neutron diffraction spectra. J. Appl. Phys. 81, 594–600. https://doi.org/10.1063/1.364220.

Mainprice, D., Bachmann, F., Hielscher, R., Schaeben, H., 2014. Descriptive tools for the analysis of texture projects with large datasets using MTEX: strength, symmetry and components. Geol. Soc., Spec. Publ. 409, 251–271. https://doi.org/10.1144/SP409.8.

Mao, W., Zhong, S., 2018. Slab stagnation due to a reduced viscosity layer beneath the mantle transition zone. Nat. Geosci. 11, 876–881. https://doi.org/10.1038/s41561-018-0225-2.

Meade, C., Silver, P.G., Kaneshima, S., 1995. Laboratory and seismological observations of lower mantle isotropy. Geophys. Res. Lett. 22, 1293–1296. https://doi.org/10.1029/95GL01091.

Merkel, S., Wenk, H.R., Badro, J., Montagnac, G., Gillet, P., Mao, H.K., Hemley, R.J., 2003. Deformation of (Mg₀.₉,Fe₀.₁)SiO₃ Perovskite aggregates up to 32 GPa. Earth Planet. Sci. Lett. 209, 351–360. https://doi.org/10.1016/S0012-821X(03)00098-0.

Miyagi, L., Merkel, S., Yagi, T., Sata, N., Ohishi, Y., Wenk, H.R., 2009. Diamond anvil cell deformation of CaSiO₃ perovskite up to 49 GPa. Phys. Earth Planet. Inter. 174, 159–164. https://doi.org/10.1016/j.pepi.2008.05.018.

Miyagi, L., Wenk, H.R., 2016. Texture development and slip systems in bridgmanite and bridgmanite + ferropericlase aggregates. Phys. Chem. Miner. 43, 597–613. https://doi.org/10.1007/s00269-016-0820-y.

Miyajima, N., Yagi, T., Ichihara, M., 2009. Dislocation microstructures of MgSiO₃ perovskite at a high pressure and temperature condition. Phys. Earth Planet. Inter. 174, 153–158. https://doi.org/10.1016/j.pepi.2008.04.004.

Montagner, J.P., Burgos, G., Capdeville, Y., Beucler, E., Mocquet, A., 2021. The mantle transition zone dynamics as revealed through seismic anisotropy. Tectonophysics 821, 229133. https://doi.org/10.1016/j.tecto.2021.229133.

Montagner, J.P., Kennett, B.L., 1996. How to reconcile body-wave and normal-mode reference Earth models. Geophys. J. Int. 125, 229–248. https://doi.org/10.1111/j.1365-246X.1996.tb06548.x.

Murakami, M., Sinogeikin, S.V., Litasov, K., Ohtani, E., Bass, J.D., 2008. Single-crystal elasticity of iron-bearing majorite to 26 GPa: implications for seismic velocity structure of the mantle transition zone. Earth Planet. Sci. Lett. 274, 339–345. https://doi.org/10.1016/j.epsl.2008.07.045.

Nisr, C., Ribárik, G., Ungár, T., Vaughan, G.B., Merkel, S., 2014. Three-dimensional x-ray diffraction in the diamond anvil cell: application to stishovite. High Press. Res. 34, 158–166. https://doi.org/10.1080/08957959.2014.885021.

Ohuchi, T., Kawazoe, T., Nishihara, Y., Nishiyama, N., Irifune, T., 2011. High pressure and temperature fabric transitions in olivine and variations in upper mantle seismic anisotropy. Earth Planet. Sci. Lett. 304, 55–63. https://doi.org/10.1016/j.epsl.2011.01.015.

Panning, M., Lekić, V., Romanowicz, B.A., 2010. Importance of crustal corrections in the development of a new global model of radial anisotropy. J. Geophys. Res., Solid Earth 115, 1–18. https://doi.org/10.1029/2010JB007520.

Panning, M., Romanowicz, B., 2006. A three-dimensional radially anisotropic model of shear velocity in the whole mantle. Geophys. J. Int. 167, 361–379. https://doi.org/10.1111/j.1365-246X.2006.03100.x.

Prescher, C., Prakapenka, V.B., 2015. DIOPTAS: a program for reduction of two-dimensional X-ray diffraction data and data exploration. High Press. Res. 35, 223–230. https://doi.org/10.1080/08957959.2015.1059835.

Ringwood, A.E., 1991. Phase transformations and their bearing on the constitution and dynamics of the mantle. Geochim. Cosmochim. Acta 55, 2083–2110. https://doi.org/10.1016/0016-7037(91)90090-R.

Rosa, A.D., Hilairet, N., Ghosh, S., Garbarino, G., Jacobs, J., Perrillat, J.P., Vaughan, G., Merkel, S., 2015. In situ monitoring of phase transformation microstructures at Earth's mantle pressure and temperature using multi-grain XRD. J. Appl. Crystallogr. 48, 1346–1354. https://doi.org/10.1107/S1600576715012765.

Schmidt, S., 2014. GrainSpotter: a fast and robust polycrystalline indexing algorithm. J. Appl. Crystallogr. 47, 276–284. https://doi.org/10.1107/S1600576713030185.

Shearer, P.M., 2000. Upper mantle seismic discontinuities. In: Karato, S.I., Forte, A., Liebermann, R., Masters, G., Stixrude, L. (Eds.), Earth's Deep Interior: Mineral Physics and To-mography from the Atomic to the Global Scale. In: Geophysical Monograph, vol. 117. American Geophysical Union, Washington, DC, USA, pp. 115–131.

Sinogeikin, S.V., Bass, J.D., 2000. Single-crystal elasticity of pyrope and MgO to 20 GPa by Brillouin scattering in the diamond cell. Phys. Earth Planet. Inter. 120, 43–62. https://doi.org/10.1016/S0031-9201(00)00143-6.

Stixrude, L., Lithgow-Bertelloni, C., 2010. Thermodynamics of mantle minerals - II. Phase equilibria. Geophys. J. Int. 184, 1180–1213. https://doi.org/10.1111/j.1365-246X.2010.04890.x.

Tateno, S., Komabayashi, T., Hirose, K., Hirao, N., Ohishi, Y., 2019. Static compression of B2 KCl to 230 GPa and its. Am. Mineral. 104, 718–723.

Tschauner, O., Chi, M., Beckett, J.R., Prescher, C., Prakapenka, V.B., Rossman, G.R., 2014. Discovery of bridgmanite, the most abundant mineral in Earth, in a shocked meteorite. Science 346, 1100–1102. https://doi.org/10.1126/science.1259369.

Tschauner, O., Huang, S., Yang, S., Humayun, M., Liu, W., Corder, S.N.G., Bechtel, H.A., Tischler, J., Rossman, G.R., 2021. Discovery of davemaoite, CaSiO₃-perovskite, as a mineral from the lower mantle. Science 374, 890–894. https://doi.org/10.1126/science.abl8568. https://www.science.org.

Tsujino, N., Nishihara, Y., Yamazaki, D., Seto, Y., Higo, Y., Takahashi, E., 2016. Mantle dynamics inferred from the crystallographic preferred orientation of bridgmanite. Nature 539, 81–84. https://doi.org/10.1038/nature19777.

Tsujino, N., Yamazaki, D., Nishihara, Y., Yoshino, T., Higo, Y., Tange, Y., 2022. Viscosity of bridgmanite determined by in situ stress and strain measurements in uniaxial deformation experiments. Sci. Adv. 8. https://doi.org/10.1126/sciadv.abm1821.

Vennari, C.E., Lin, F., Kunz, M., Akaogi, M., Miyagi, L., Williams, Q., 2021. Deformation and strength of mantle relevant garnets: implications for the subduction of basaltic-rich crust. Am. Mineral. 106, 1045–1052. https://doi.org/10.2138/am-2021-7587.

Visser, K., Trampert, J., Lebedev, S., Kennett, B.L., 2008. Probability of radial anisotropy in the deep mantle. Earth Planet. Sci. Lett. 270, 241–250. https://doi.org/10.1016/j.epsl.2008.03.041.

Wang, B., Niu, F., 2010. A broad 660 km discontinuity beneath northeast China revealed by dense regional seismic networks in China. J. Geophys. Res., Solid Earth 115, 1–12. https://doi.org/10.1029/2009JB006608.

Wang, X., Tsuchiya, T., Hase, A., 2015. Computational support for a pyrolitic lower mantle containing ferric iron. Nat. Geosci. 8, 556–559. https://doi.org/10.1038/ngeo2458.

Waszek, L., Tauzin, B., Schmerr, N.C., Ballmer, M.D., Afonso, J.C., 2021. A poorly mixed mantle transition zone and its thermal state inferred from seismic waves. Nat. Geosci. 14, 949–955. https://doi.org/10.1038/s41561-021-00850-w.

Wenk, H.R., Ischia, G., Nishiyama, N., Wang, Y., Uchida, T., 2005. Texture development and deformation mechanisms in ringwoodite. Phys. Earth Planet. Inter. 152, 191–199. https://doi.org/10.1016/j.pepi.2005.06.008.

Wenk, H.R., Lonardeli, I., Pehl, J., Devine, J., Prakapenka, V., Shen, G., Mao, H.K., 2004. In situ observation of texture development in olivine, ringwoodite, magnesiowüstite and silicate perovskite at high pressure. Earth Planet. Sci. Lett. 226, 507–519. https://doi.org/10.1016/j.epsl.2004.07.033.

Wenk, H.R., Lonardelli, I., Merkel, S., Miyagi, L., Pehl, J., Speziale, S., Tommaseo, C.E., 2006. Deformation textures produced in diamond anvil experiments, analysed in radial diffraction geometry. J. Phys. Condens. Matter 18, S933–S947. https://doi.org/10.1088/0953-8984/18/25/S02.

Wookey, J., Kendall, J.M., Barruol, G., 2002. Mid-mantle deformation inferred from seismic anisotropy. Nature 415, 777–780. https://doi.org/10.1038/415777a.

Xu, F., Vidale, J.E., Earle, P.S., 2003. Survey of precursors to PP: fine structure of mantle discontinuities. J. Geophys. Res., Solid Earth 108. https://doi.org/10.1029/2001jb000817. ETG 7–1–ETG 7–10.

Yamazaki, D., Yoshino, T., Matsuzaki, T., Katsura, T., Yoneda, A., 2009. Texture of (Mg,Fe)SiO₃ perovskite and ferro-periclase aggregate: implications for rheology of the lower mantle. Phys. Earth Planet. Inter. 174, 138–144. https://doi.org/10.1016/j.pepi.2008.11.002.

Yang, J., Lin, J.F., Jacobsen, S.D., Seymour, N.M., Tkachev, S.N., Prakapenka, V.B., 2016. Elasticity of ferropericlase and seismic heterogeneity in the Earth's lower mantle. J. Geophys. Res., Solid Earth 121, 8488–8500. https://doi.org/10.1002/2016JB013352.

Yuan, K., Beghein, C., 2013. Seismic anisotropy changes across upper mantle phase transitions. Earth Planet. Sci. Lett. 374, 132–144. https://doi.org/10.1016/j.epsl.2013.05.031.

Zhou, W.Y., Zhang, J.S., Huang, Q., Lai, X., Chen, B., Dera, P., Schmandt, B., 2022. High pressure-temperature single-crystal elasticity of ringwoodite: implications for detecting the 520 discontinuity and metastable ringwoodite at depths greater than 660 km. Earth Planet. Sci. Lett. 579, 117359. https://doi.org/10.1016/j.epsl.2021.117359.